CD56/NCAM mediates cell migration of human NK cells by promoting integrin-mediated adhesion turnover

Amera L. Martinez[a,†,‡], Michael J. Shannon[a,‡], Tyler Sloan[b], and Emily M. Mace[a,*]

[a]Department of Pediatrics, Vagelos College of Physicians and Surgeons, Columbia University Medical Center, New York, NY 10024; [b]Quorumetrix Solutions, Montreal, QC H1T 2H5

ABSTRACT Natural killer (NK) cells patrol tissue to mediate lysis of virally infected and tumorigenic cells. Human NK cells are typically identified by their expression of neural cell adhesion molecule (NCAM, CD56), yet despite its ubiquitous expression on NK cells, CD56 remains a poorly understood protein on immune cells. CD56 has been previously demonstrated to play roles in NK cell cytotoxic function and cell migration. Specifically, CD56-deficient NK cells have impaired cell migration on stromal cells and CD56 is localized to the uropod of NK cells migrating on stroma. Here, we show that CD56 is required for NK cell migration on ICAM-1 and is required for the establishment of persistent cell polarity and unidirectional actin flow. The intracellular domain of CD56 (NCAM-140) is required for its function and the loss of CD56 leads to enlarged actin foci and sequestration of phosphorylated Pyk2 accompanied by increased size and frequency of activated LFA-1 clusters. Together, these data identify a role for CD56 in regulating human NK cell migration through modulation of actin dynamics and integrin turnover.

SIGNIFICANCE STATEMENT

- NCAM/CD56 is highly expressed on human natural killer (NK) cells but has a poorly described function.
- The authors observed that deletion of CD56/NCAM on human NK cells leads to impaired cell migration and dysregulated actin features.
- These results suggest that impaired cell migration in CD56/NCAM-deficient cells is associated with increased LFA-1 activation.

INTRODUCTION

Expression of CD56 (NCAM) marks human natural killer (NK) cells and uniquely demarcates human NK cell subsets (Lanier *et al.*, 1989, 1991). CD56/NCAM is a member of the Ig superfamily that has been best characterized on neurons and plays roles in cell adhesion, axon guidance, and synaptic function (Sytnyk *et al.*, 2017). CD56/NCAM is commonly expressed in three primary isoforms. While the extracellular domain is conserved between all its isoforms, the NCAM-120 isoform has a GPI anchor and NCAM-140 and -180 isoforms have intracellular domains of varying length. Signaling from CD56 has been poorly characterized in lymphocytes, however in

neurons each of the NCAM isoforms can influence downstream signaling through direct and indirect binding. Signaling pathways downstream of NCAM in neurons include a constitutive association of NCAM-140 with p59[fyn] in axonal growth cones which leads to recruitment of focal adhesion kinase (FAK) upon NCAM cross-linking (Beggs *et al.*, 1997). This pathway is of particular interest given the expression of the FAK homologue Pyk2 in human NK cells and decreased Pyk2 phosphorylation in CD56-knockout (KO) NK cells (Gunesch *et al.*, 2020). Expression of CD56 on human NK cell lines promotes cytotoxic function and cytokine secretion, and previous studies have identified decreased Pyk2 phosphorylation resulting from deletion of CD56 on human NK cell lines (Gunesch *et al.*, 2020). Cross-linking with anti-CD56 antibodies on NK cells promotes signaling in cytokine activated NK cells, further linking it to functional outcomes mediated by intracellular signaling (Picard *et al.*, 2022).

In addition to its role in cytotoxicity, CD56/NCAM is implicated in the migration and differentiation of human NK cells (Mace *et al.*, 2016). Primary human NK cells undergo spontaneous cell migration on stromal cell monolayers used to support NK cell differentiation from hematopoietic precursors (Mace *et al.*, 2016; Lee and Mace, 2017; Lee *et al.*, 2020a). These stromal cells are often a heterogeneous mix of endothelial and mesenchymal cells that express cell adhesion ligands including VCAM-1 and CD44 and secrete extracellular matrix components, including collagen (Lee *et al.*, 2020a, Charbord *et al.*, 2002 #34). Deletion of CD56/NCAM on primary NK cells or the NK92 NK cell line impairs cell migration on EL08.1D2 stromal cells (Mace *et al.*, 2016), however the ligands mediating interactions between NK cells and stromal cells have not been elucidated. In addition to ligands for integrins, EL08.1D2 cells express NCAM, and homotypic (NCAM-NCAM) interactions *in trans* can induce signaling and cell migration in neuronal cells (Sandig *et al.*, 1994). It has remained unclear whether the previously described interactions between NK cells and stromal cells were mediated by NCAM-NCAM adhesion or by other receptor-ligand interactions. Here, we sought to measure cell migration on ICAM-1, a well-defined integrin ligand of LFA-1, to interrogate the role of CD56/NCAM in NK cell migration independently of NCAM-NCAM interactions.

Lymphocyte cell migration is amoeboid motility regulated by cell adhesion, activation of actomyosin contractility, and actin remodeling, coupled with cell polarity (Dupre *et al.*, 2015). While lymphocytes initially undergo symmetrical spreading on ICAM-1, the continuous actin remodeling that occurs on ICAM-1 coated surfaces, even in the absence of a chemokine gradient or shear flow, leads to symmetry breaking and cell migration in both T-cells and NK cells (Sims *et al.*, 2007; Culley *et al.*, 2009; Kumari *et al.*, 2020). Cell polarity in migrating lymphocytes includes the formation of a leading edge and a trailing edge, or uropod. We have previously shown that CD56/NCAM localizes to the uropod of human NK cells migrating on stromal cells (Mace *et al.*, 2016). Uropod localization is not unusual for adhesion receptors and glycoproteins, and other proteins, including CD44 and VLA-4 (integrin α4β1), are similarly localized and play a role in signaling for cell migration and polarity (Mrass *et al.*, 2008). The FAK homologue Pyk2 is also localized to the trailing edge of migrating NK cells and translocates to the immune synapse upon target cell contact (Sancho *et al.*, 2000). Pyk2 has multiple sites of tyrosine phosphorylation, including the autophosphorylation site Y402, and phospho-Pyk2 Y881 is predominantly found in the uropod and mediates integrin detachment from substrates to enable T-cell migration (Cheung and Ostergaard, 2016).

Here, we sought to better understand the underlying mechanism for impaired cell migration in CD56-deficient human NK cells. Given the role of LFA-1 in promoting cell polarization and spontaneous NK cell migration (Culley *et al.*, 2009), we studied spontaneous NK cell migration on immobilized ICAM-1 surfaces by confocal and structured illumination microscopy (SIM) of NK92 cell lines. Through careful dissection of the effect of CD56 deletion in NK92 cells, including the use of NK cell lines expressing actin reporters, we identify new roles for CD56/NCAM in regulating actin and integrin function in migrating lymphocytes.

RESULTS

Localization of CD56/NCAM in human NK cells

CD56/NCAM has been previously described to be found in the uropod in primary human NK cells migrating on stromal cells (Mace *et al.*, 2016); however, its spatial localization in relation to other proteins associated with cell migration has not been fully explored. To investigate the cellular localization of CD56/NCAM further, we performed fixed cell confocal microscopy of primary NK cells and the human NK cell line NK92 spontaneously migrating on ICAM-1 coated surfaces. As previously described for cells migrating on stromal cell monolayers (Mace *et al.*, 2016), CD56/NCAM was found in the uropod, which was marked by enrichment of CD44 in primary NK cells and NK92 cells (Figure 1, A and B). While less intense than the localization within the uropod, we also found CD56 localized at the membrane in regions of actin enrichment, including at the leading edge of migrating cells (Figure 1, A and B). Line profiles underscored the association between CD56/NCAM and the uropod and leading edge of the cell, whereas CD44 was exclusively localized to the cell uropod (Figure 1C). This relationship was quantified by measuring the fluorescence of CD56 and CD44 at the leading edge and uropod. While both were significantly enriched in the uropod, this enrichment was greater for CD44 than for CD56 (Figure 1D).

CD56/NCAM deletion impairs spontaneous cell migration on ICAM-1

Deletion of CD56 in the NK92 cell line impairs NK cell migration on EL08.1D2 stromal cells (Mace *et al.*, 2016), however the adhesion receptors that mediate spontaneous migration on stroma are not well-defined and could include NCAM itself (Sandig *et al.*, 1994). To evaluate cell migration on isolated integrin ligand and exclude binding to NCAM as a mechanism for CD56-mediated migration, we incubated wild-type and CD56-KO NK92 cells on Fc-ICAM-1 coated surfaces to induce spontaneous crawling migration. Cells were imaged by live cell phase contrast microscopy at 20X magnification using a large field of view. As manual tracking of many cells is time-consuming and can lead to biased measurements, we segmented cells using Cellpose (Stringer *et al.*, 2021) and linked cells between frames using Bayesian tracker (Ulicna *et al.*, 2021; Figure 2, A and B). Unlike WT NK92 cells, CD56-KO NK92 cells had impaired migration, yet appeared dynamic and could be seen forming cell protrusions while failing to undergo polarized and directional migration (Figure 2, A and B,; Supplemental Movies 1 and 2). We additionally noted elongated morphologies, including stretched uropods, of CD56-KO NK92 cells that failed to significantly migrate during the time of imaging (arrowheads, Figure 2B).

Cell segmentation and tracking were followed by analysis using a new custom software pipeline to measure 24 parameters of cell morphology, migration, and cell clustering (Shannon *et al.*, 2023). Consistent with a role for CD56/NCAM in mediating NK92 cell migration, we found decreased migratory capacity of CD56-KO cells when Euclidean distance and speed were considered (Figure 2, C and D)
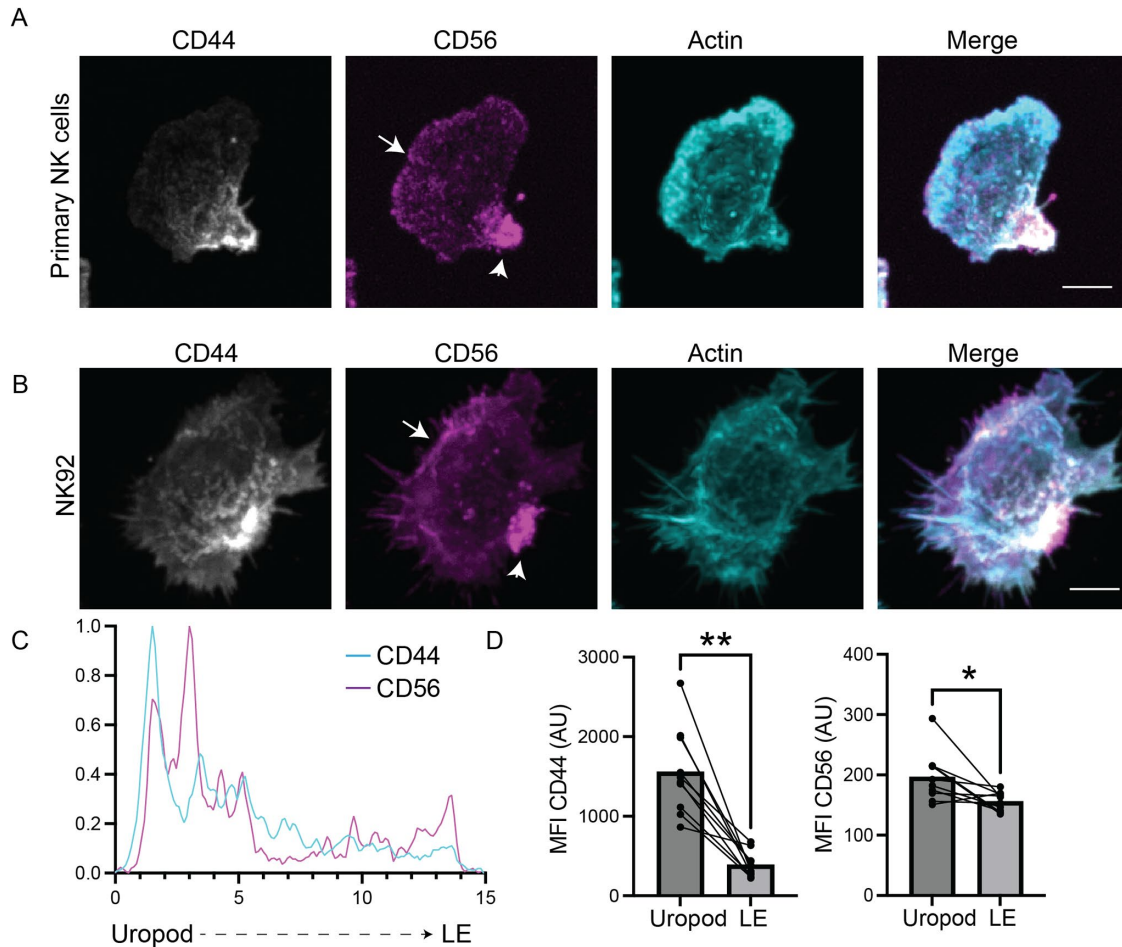
FIGURE 1: Localization of CD56/NCAM with actin and in the uropod of migrating human NK cells. (A) Primary human NK cells undergoing spontaneous migration on immobilized ICAM-1 were fixed, immunostained and imaged by confocal microscopy as indicated. Representative image from 40 fields of view from three biological and technical replicates. (B) NK92 cells undergoing spontaneous migration on immobilized ICAM-1 were fixed, immunostained, and imaged by confocal microscopy. Representative image from 35 fields of view from three technical replicates (C) Representative mean fluorescence intensity (MFI) of CD56/NCAM (magenta) or CD44 (cyan) along the cell axis from the cell posterior (uropod) to the leading edge (LE) of a representative primary NK cell from 40 fields of view (three biological replicates). Scale bars 5 µm. (D) Quantification of CD56/NCAM (left) and CD44 (right) MFI at the uropod and leading edge (LE) from 10 primary NK cells from one representative experiment from three biological replicates; bars represent mean values. AU, arbitrary units; **$p = 0.002$, *$p = 0.0137$, Wilcoxan matched-pairs signed rank test.

and increased arrest coefficient (Figure 2E). CD56-KO cells had greater cell area and aspect ratio when compared with WT cells (Figure 2, F and G), reflecting the cell stretching described above. In addition, CD56-KO cells formed homotypic cell clusters less frequently as measured by Ripley's L (r) coefficient (Figure 2H).

Our measurements were complemented by related descriptors of cell and migration features, and we additionally found increased cell perimeter, and decreased mean squared displacement (MSD), maximum distance, and cumulative length in CD56-KO cells relative to WT cells (Supplemental Figure 1). These measurements were consistently stable over the time of imaging, thus confirming that our imaging timescales were appropriately capturing cell behaviors (Supplemental Figure 2). To confirm that the spontaneous migration we observed was specific to ICAM-1, we included control surfaces coated with Fc only, poly-L-lysine, or anti-CD18 to induce LFA-1 cross-linking. While anti-CD18 induced cell spreading in both WT and CD56-KO cells, quantified by increased cell area, none of these surfaces induced significant spontaneous cell migration (Supplemental Figure 3).

CD56-KO NK92 cells have decreased unidirectional persistence of actin flow and fail to maintain cell polarity

To investigate the reduced capacity for cell migration by CD56-KO cells further, we imaged WT and CD56-KO NK92 cells expressing LifeAct mScarlet (Bindels et al., 2017) using higher resolution (100X) live cell confocal microscopy. Confocal imaging of actin in live cells confirmed unidirectional polarization and migration of WT NK92 cells, characterized by a dynamic branched actin network at the leading edge, and revealed the multidirectional formation of actin networks in CD56-KO NK92 cells (Figure 3A; Supplemental Movies 3 and 4). To quantify this observation, we used particle image velocimetry (PIV) for visualization of actin flow (Wheatley et al., 2022). To quantify changes in actin flow directionality, we extracted the kappa parameter from a Von Mises fit of 10 s overlapping time windows of flow. This analysis demonstrated that CD56-KO NK92 cells are not able to maintain a directionally persistent flow in the leading edge (Figure 3, B and C). Despite their impaired cell migration (Figures 2 and 3D), CD56-KO cells had only slightly decreased actin flow speeds
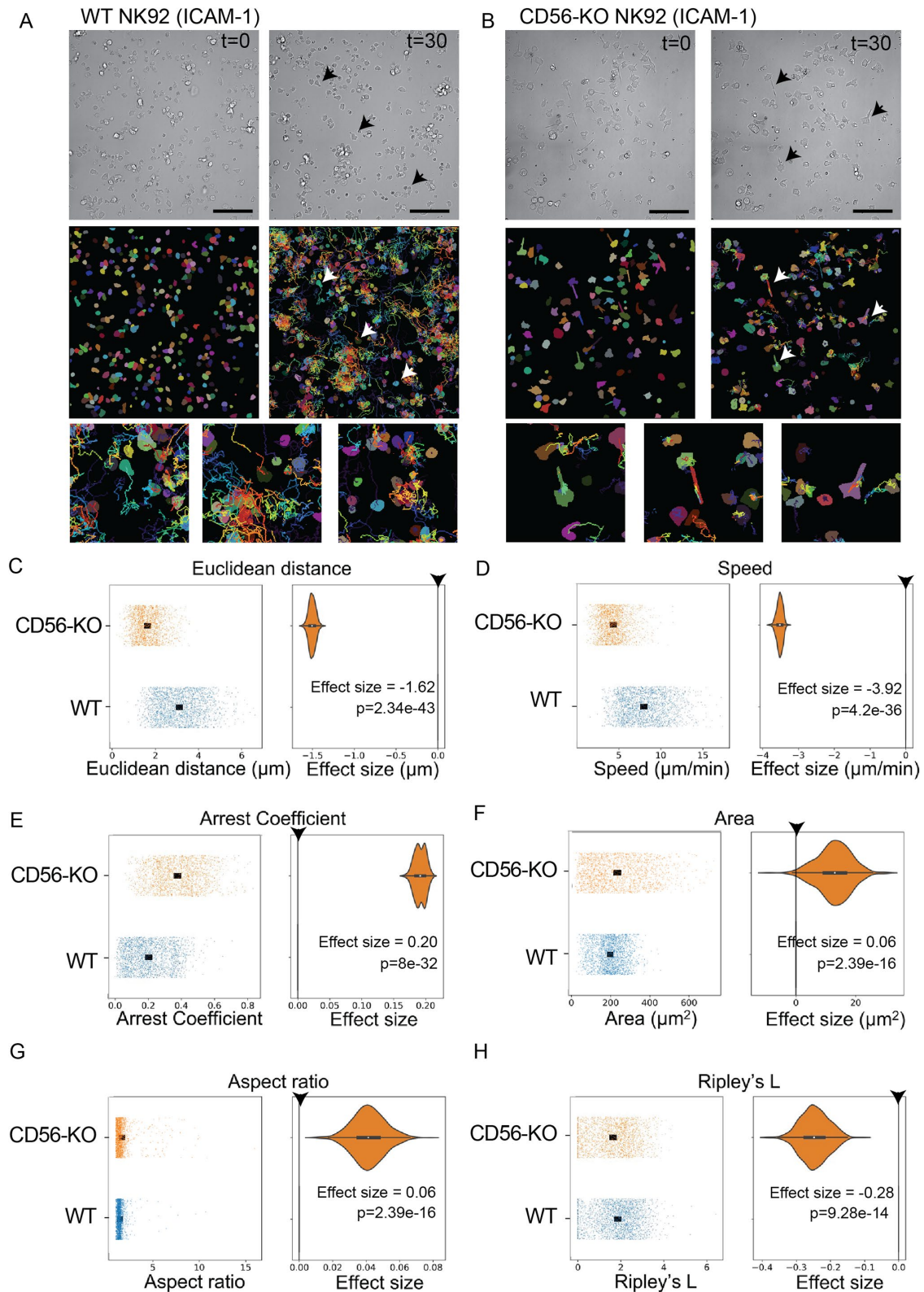
FIGURE 2: CD56 deletion slows cell migration, decreases cell clustering, and increases cell area. WT or CD56-KO NK92 cells were incubated on ICAM-1 coated glass and imaged by live cell phase contrast microscopy at 10 s intervals for 30 min. (A and B) Representative micrographs and segmentation by Cellpose that preceded tracking using btrack. Examples indicated by arrowheads are magnified in the bottom panel. (C–H) Plots of Difference show the distribution of the data (left pane) and effect size (right pane) for metrics related to migration, morphology, and clustering: (C) Euclidean distance, (D) speed, (E) arrest coefficient, (F) area, (G) aspect ratio, and (H) Ripley's L (clusteredness). n = 3574 (WT) and 2945 (CD56-KO) cells pooled from five technical replicates. Cells included in the analysis were

(Figure 3E) and similar immobile actin fractions (Figure 3F) as WT NK92 cells, described statistically using a distribution of the effect size on the right side of the plot. Larger distances of the median effect size from the control line at zero coupled with a tighter distribution suggest more substantial biological effects, and no overlap of the effect size distribution with the control line typically indicates a statistically significant difference from the control. Performing the same PIV analysis on actin flow in NK cells incubated on anti-CD18 functionalized surfaces demonstrated extensive actin remodeling in both WT and CD56-KO cells, however actin remodeling occurred at multiple or extended lamellipodia on anti-CD18 and the cells did not polarize or migrate (Supplemental Figure 4; Supplemental Movies 5 and 6). CD56-KO cells on anti-CD18 did exhibit a very slightly reduced directional persistence of actin flow, reflecting disordered actin dynamics, but due to the existence of multiple lamellipodia in the WT cells on this surface, the difference was minimal (Supplemental Figure 4). Actin remodeling effects were demonstrated to be specific, as treatment with cytochalasin D significantly reduced actin flow speed in both cell types (Supplemental Figure 5) and were constant over the 2-min timelapse imaging period in all cases (Supplemental Figure 6). Therefore, while anti-CD18 induces actin remodeling, ICAM-1 uniquely promotes symmetry breaking and spontaneous cell migration. Further, while persistent unidirectional actin flow and maintenance of the leading edge is dependent on CD56/NCAM function, actin remodeling occurs in both WT and CD56-KO lines.

We performed SIM on cells migrating on ICAM-1 to understand how the fine structure of actin fibers are affected by CD56 deficiency. While WT NK92 cells were polarized with a clear leading and trailing edge, CD56-KO NK92 cells often had multipolar phenotypes, and many were either contracted with no clear polarity or elongated as previously observed in live cell imaging (Figure 3G). Quantification of the frequency of cells that formed single or multiple leading-edge structures showed a significantly greater frequency of CD56-KO NK92 cells with >1 leading edge than WT cells, and a slightly greater frequency of CD56-KO NK92 cells with no apparent leading edge (Figure 3H). To further validate this observation, we imaged WT and CD56-KO lines in collagen matrices by lattice light-sheet microscopy at high temporal and spatial resolution. Live cell imaging of both WT and CD56-KO LifeAct mScarlet NK92 lines revealed dynamic actin processes of cells in collagen, however whereas WT cells were polarized and exhibited flat lamellar projections, CD56-KO NK92 cells were less polarized and had multidimensional projections (Figure 3I; Supplemental Movies 7 and 8).

Together with cell migration data, these data demonstrate that CD56-KO NK92 cells have impaired cell migration and an inability to maintain a persistent leading edge, but that their capacity for dynamic actin remodeling is not significantly impaired.

The intracellular domain of CD56 is required for actin homeostasis

We noted the presence of dynamic actin foci in the mid-body of cells in both WT and CD56-KO LifeAct mScarlet NK92 cells incubated on ICAM-1 that were more pronounced in CD56-KO NK92 cells (Supplemental Movies 3 and 4). Our SIM imaging also showed that CD56-KO cells migrating on ICAM-1 had larger actin foci and

longer filopodia than WT NK92 cells (Figure 3G). Similar structures were observed in WT and CD56-KO NK92 cells incubated on anti-CD18 antibody, which induces symmetrical spreading but not cell migration (Supplemental Movies 5 and 6). Our previous study has demonstrated the presence of CD56/NCAM at the NK cell immunological synapse, where it is colocalized with actin (Gunesch et al., 2020). To model actin remodeling in response to co-ligation of integrin and activating receptors, we combined anti-CD18 with anti-NKp30 ligation on functionalized glass (Rak et al., 2011). This approach enabled us to focus on the pronounced actin foci in CD56-KO NK cells undergoing symmetrical spreading and to look more closely at these structures in the absence of cell polarity and symmetry breaking (Figure 4A). Three-dimensional reconstruction of these images showed that actin foci in CD56-KO cells were taller in the Z dimension as well as XY (Figure 4B) and further highlighted the presence of filopodia seen in XY imaging at the plane of the glass.
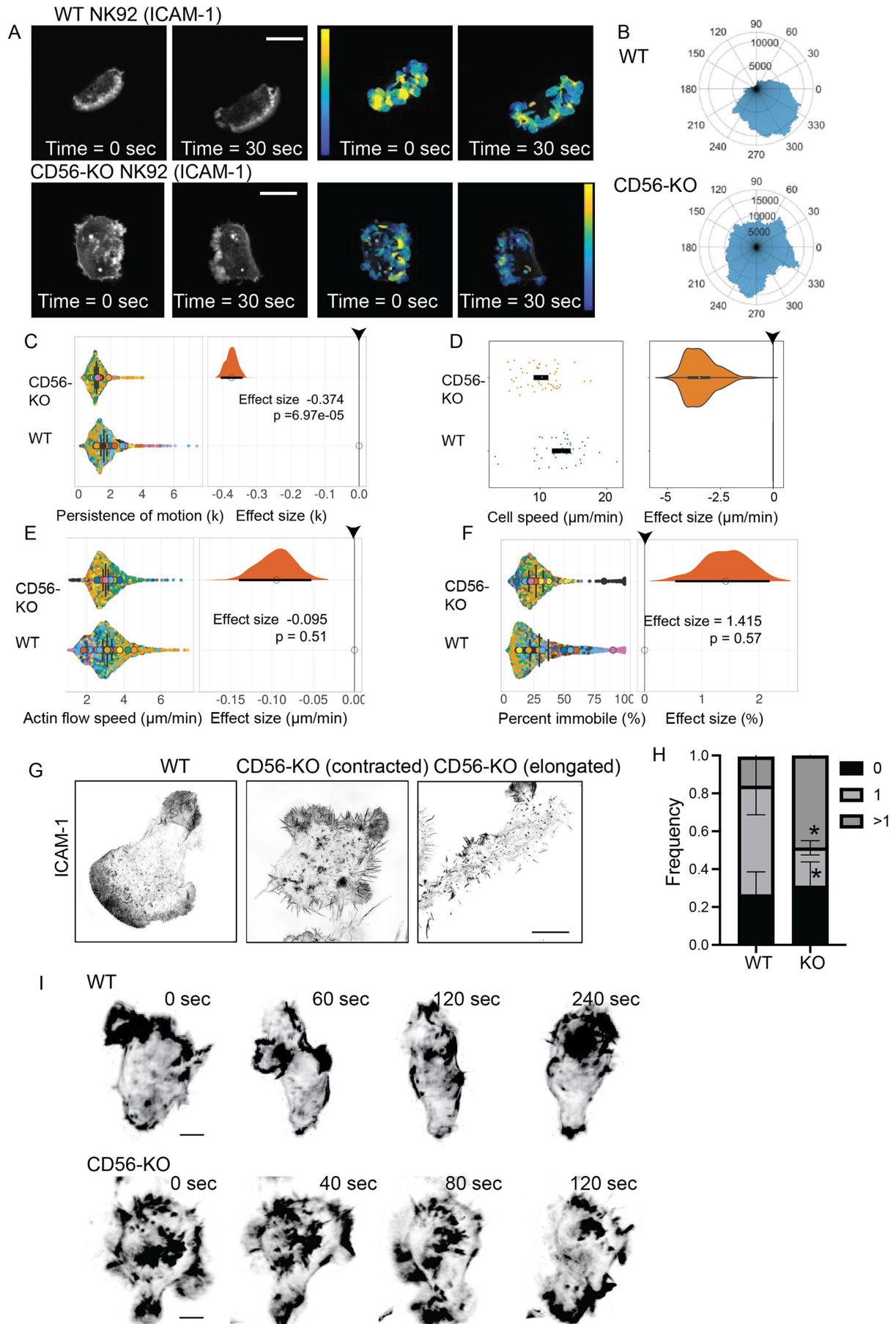
Given the distinctive actin structures seen in CD56-KO NK92 cells, we hypothesized that CD56/NCAM may be mediating actin remodeling via its intracellular domain. CD56/NCAM is expressed as three common isoforms, and the NCAM-140 isoform is predominantly expressed in human NK cells (Lanier et al., 1989, 1991; Moebius et al., 2007; Gunesch et al., 2020). We reconstituted CD56-KO NK92 cells with full-length NCAM-140 or NCAM-140 lacking its intracellular domain (ΔICD) (Gunesch et al., 2020). Flow cytometry confirmed the surface expression of CD56/NCAM in all reconstituted lines (Figure 4C). Probing by Western blot confirmed that the molecular weight of the full-length construct corresponded to WT CD56/NCAM, whereas the truncated isoform had decreased molecular weight predicted by the loss of the intracellular domain (Figure 4D). To determine whether the intracellular signaling domain of CD56/NCAM-140 is required to mediate actin homeostasis, we incubated CD56-KO cells that had been reconstituted with full-length or truncated (ΔICD) CD56/NCAM on anti-CD18 coated surfaces and measured the accumulation of actin foci using SIM. As shown in Figure 4A, CD56-KO cells had significantly larger actin foci than WT NK92 (Figure 4E). As predicted, cells expressing full-length CD56 had actin foci that were not significantly different in size from WT NK92 cells. Cells expressing the truncated (ΔICD) form of CD56 had actin foci that were enlarged, and actin foci areas in these cells were not significantly different from the CD56-KO condition (Figure 4E). Similarly, actin filopodia length was restored in CD56-KO NK92 cells expressing the full-length 140 kDa isoform, but not ΔICD, of CD56 (Figure 4E). Quantification confirmed the significantly increased size of actin foci and increased length of filopodia, and the rescue of these effects by full-length, but not truncated, CD56/NCAM-140 (Figure 4F). Together these data demonstrate that the role that CD56/NCAM-140 plays in regulating actin phenotypes is dependent on the intracellular domain of NCAM-140.

Impaired integrin adhesion turnover in CD56-KO cells is associated with changes in Pyk2 Y402 and Pyk2 Y881 localization

Previous studies have shown that CD56 deletion leads to decreased phosphorylation of the protein tyrosine kinase Pyk2 (Gunesch et al., 2020) and that Pyk2 can play a role in uropod detachment and

---

filtered to include at least 2 min of tracking and a minimal area of 10 μm^2 to exclude cell debris. Arrowheads on Plots of Differences indicates zero line for control condition (WT NK92); median values are shown ± 95% confidence intervals for Plots of Differences and their effect sizes. Each datapoint is a cell. P values were calculated by unpaired t test and effect sizes were calculated as described in detail in *Materials and Methods*.

WT NK92 (ICAM-1)

A

Time = 0 sec   Time = 30 sec   Time = 0 sec   Time = 30 sec

CD56-KO NK92 (ICAM-1)

Time = 0 sec   Time = 30 sec   Time = 0 sec   Time = 30 sec

B

WT

CD56-KO

C

CD56-KO

WT

Effect size -0.374
p =6.97e-05

Persistence of motion (k)   Effect size (k)

D

CD56-KO

WT

Cell speed (µm/min)   Effect size (µm/min)

E

CD56-KO

WT

Effect size -0.095
p = 0.51

Actin flow speed (µm/min)   Effect size (µm/min)

F

CD56-KO

WT

Effect size = 1.415
p = 0.57

Percent immobile (%)   Effect size (%)

G

ICAM-1

WT   CD56-KO (contracted) CD56-KO (elongated)

H

Frequency

WT   KO

0
1
>1

I

WT

0 sec   60 sec   120 sec   240 sec

CD56-KO

0 sec   40 sec   80 sec   120 sec

lymphocyte migration, particularly through phosphorylation on the Y881 motif (Cheung and Ostergaard, 2016). As previously reported in cytotoxic T lymphocytes, we found that Pyk2 phospho-Y881 was localized to the uropod of NK92 cells migrating on ICAM-1 coated surfaces (Figure 5A). In contrast, Pyk2 phospho-Y402 was more diffusely localized and there was a smaller pool of Pyk2 phospho-Y402 also found in the uropod (Figure 5A). CD56-KO NK92 cells formed multipolar patterns on ICAM-1 as previously shown, including large actin foci. These foci were highly enriched for Pyk2 phospho-Y402 in CD56-KO, but not WT, NK92 cells (Figure 5A, right). In contrast, we did not observe enrichment of actin with phospho-Pyk2 Y881 in WT or CD56-KO cells. Line profiles across pPyk2 foci further demonstrated enrichment of actin in Pyk2 phospho-Y402 (Figure 5B, right), but not phospho-Y881 (Figure 5B, left), foci in CD56-KO NK92 cells (Figure 5B). While phospho-Pyk2 Y881 was mainly restricted to the uropod in WT cells, its distribution appeared more diffuse in CD56-KO cells and quantification of the area of phospho-Pyk2 Y881 immunofluorescence confirmed consistently increased area of phospho-Pyk2 Y881 in CD56-KO cells compared with WT cells (Figure 5C).

The presence of multiple lamellipodial structures in CD56-KO cells suggested that establishment of cell polarity was impaired in CD56-KO cells attempting to migrate on ICAM-1 coated surfaces. Alternatively, the presence of actin foci enriched for phospho-Pyk2 suggested that dysregulation of integrin-mediated adhesion turnover may be a driver of this phenotype. To distinguish between these two mechanisms, we detected phospho-ERM (pERM) proteins, as these are also associated with establishing cell polarity in migrating lymphocytes. In both WT and CD56-KO NK92 cells we found ERM phospho-Thr558 in a localized patch in cells on ICAM-1 (Figure 5D). In WT cells, this patch of pERM was localized in the cell uropod. The presence of multilamellar structures made it more difficult to identify a clear uropod in CD56-KO NK92 cells, however the presence of clustered pERM suggests that initial signaling to generate cell polarity on ICAM-1 is preserved. We did note, however, that the area of pERM detected in CD56-KO NK92 cells was reproducibly greater than in WT NK92 cells (Figure 5E). This observation, which was similar to what we observed for phospho-Pyk2 Y881, suggests that CD56 may be playing a role in constraining ERM proteins.

Finally, in neurons CD56/NCAM is associated with the Src kinase Fyn, which is also expressed in lymphocytes and mediates NK cell effector functions and T-cell chemotaxis (Lowin-Kropf *et al.*, 2002; Schaeuble *et al.*, 2011). To determine whether loss of CD56/NCAM affected Fyn localization or phosphorylation, we immunostained for phospho-Fyn in WT and CD56-KO NK92 cells migrating on ICAM-1 (Figure 5F). We found that phospho-Fyn was similarly localized to the uropod of migrating cells, and loss of CD56/NCAM similarly led to increased area of phospho-Fyn in CD56-KO cells (Figure 5G). These observations suggest that polarity induced by ERM protein and Fyn phosphorylation is not disrupted upon loss of CD56/NCAM but that CD56 may be playing a role in constraining polarity proteins following cell polarization.

Loss of CD56/NCAM leads to an increase in activated LFA-1 on the cell surface

Given the apparent differences in integrin-mediated adhesion and intact cell polarity signaling in CD56-KO cells, we investigated the structure of LFA-1 focal complexes in NK92 cells migrating on ICAM-1. Detection of open conformation LFA-1 by confocal microscopy using the monoclonal antibody m24 identified a greater number of high-affinity LFA-1 foci with a greater area and intensity in CD56-KO NK92 cells on ICAM-1 when compared with WT cells (Figure 6, A and B). Reconstruction of three-dimensional images from Z-stacks supported this observation and identified enrichment of m24 staining in the glass-proximal slices in CD56-KO NK92 cells relative to WT (Figure 6A, right). Flow cytometry confirmed that total cell surface expression of β2 integrin (CD18) was not affected by loss of CD56/NCAM (Figure 6C).

As detection of active LFA-1 foci by confocal microscopy was constrained by the diffraction limit, we additionally imaged active LFA-1 on NK92 cells on ICAM-1 using SIM (Figure 6D). This approach allowed us to measure the area of high affinity LFA-1, which identified a larger size of foci in CD56-KO NK92 cells relative to WT cells (Figure 6E). This observation, together with larger phospho-Pyk2 enriched actin foci in CD56-KO cells, suggests that integrin-mediated adhesions are not being appropriately disassembled in CD56-KO NK92 cells.

FIGURE 3: Lamellipodial actin flow polarity is deficient while flow speed is intact in CD56-KO NK92 cells migrating on ICAM-1. WT or CD56-KO NK92 cells expressing LifeAct mScarlet were incubated on ICAM-1 coated glass and imaged by live cell confocal microscopy at 100X magnification for 2 min per field of view with 1 s between frames using a 561-nm laser. See also Supplemental Movies 3 and 4. (A) Example frames from a timelapse movie are shown at 0 and 30 s (left) with Lucas-Kanade PIV vector field (right); warm colors = high magnitude, cold = low. Representative of 39 cells (WT) and 37 cells (CD56-KO) from three technical replicates. (B) Polar histogram of directionality of PIV vectors. (C) Plots of difference showing the persistence of motion of flow (κ from the von Mises fit) across 10 s overlapping time windows illustrating change in flow direction. Each datapoint represents a measurement from a discrete time window with cells coded by color, large datapoints represent mean of each cell. (D) Plots of difference of cell speed of migration. Each datapoint represents a cell. (E) Plots of difference of actin flow speed. Each datapoint represents a measurement from a discrete time window with cells coded by color, large datapoints represent mean of each cell. (F) Percent of actin fraction that was immobile. Each datapoint represents a measurement from a discrete time window with cells coded by color, large datapoints represent mean of each cell. $n = 27$ (WT) and 25 (CD56-KO) cells from three technical replicates (C–F). *P* values calculated by unpaired *t* test. Arrowhead indicates zero line for control condition (WT NK92) on plots of difference; median values are shown $\pm$ 95% confidence intervals for plots of differences and their effect sizes (C–F). (G) WT or CD56-KO NK92 cells migrating on ICAM-1 were fixed, immunostained for actin (phalloidin) and imaged by SIM. Representative of 28 cells (WT) and 27 cells (CD56-KO) from four technical replicates. Scale bar 5 μm. (H) WT or CD56-KO NK92 cells migrating on ICAM-1 were manually scored for the fraction of cells with 0, 1, or >1 lamellipodia. Mean $\pm$ SD of the average fraction from three independent confocal microscopy experiments, $n = 150$ (WT) and 262 (CD56-KO). *$p < 0.05$ by Sidak's multiple comparisons test (WT-KO 1 and >1 conditions, 0 condition = not significant). (I) Lattice lightsheet imaging of WT or CD56-KO NK92 cells expressing LifeAct mScarlet embedded in 1.6 mg/ml collagen and imaged live every 40 s. Select frames are shown to highlight cell morphologies; see also Supplemental Movies 7 and 8. Representative of 20 cells (WT) and 12 cells (CD56-KO) from four technical replicates. Scale bar 5 μm.
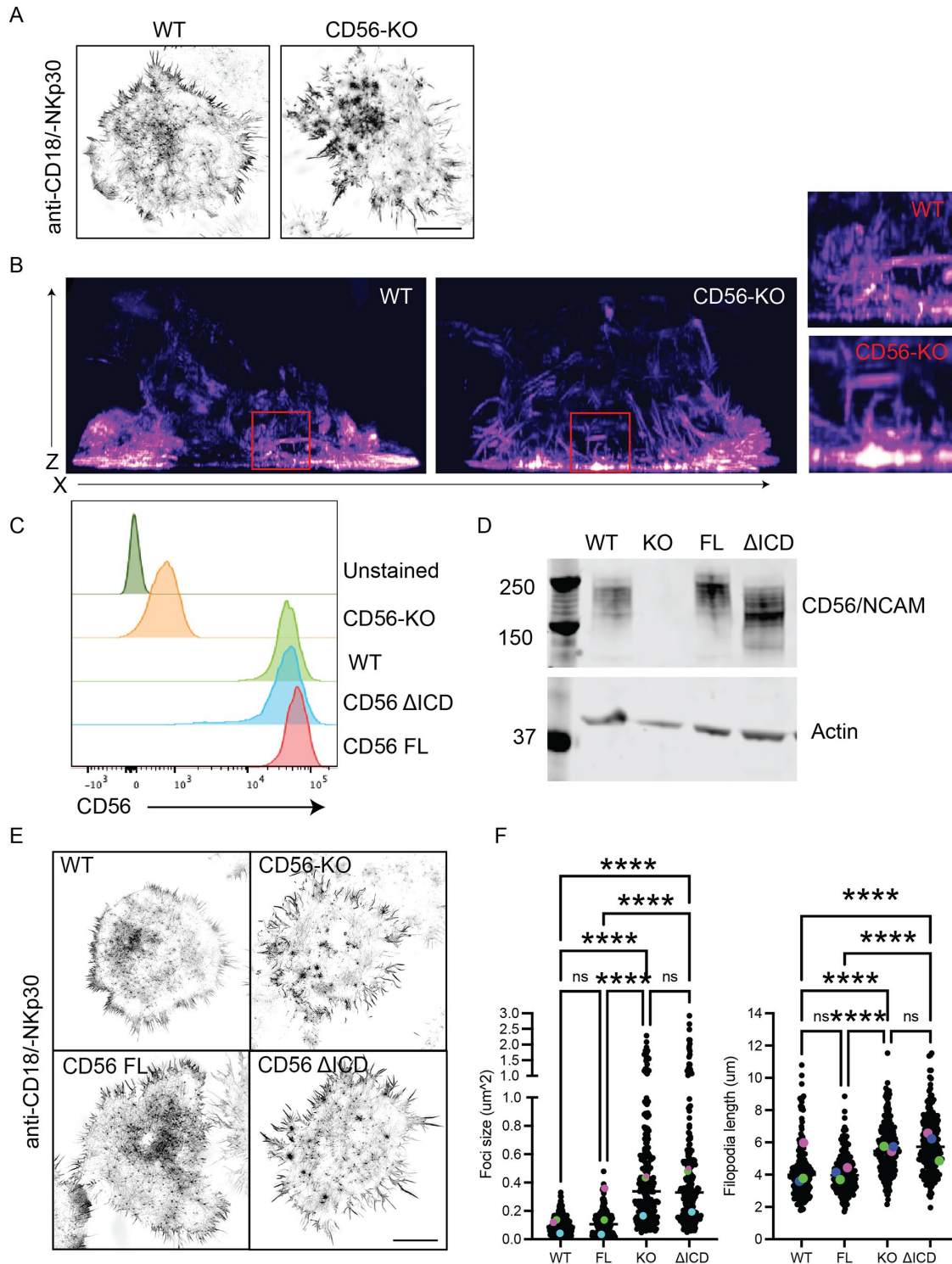
FIGURE 4: The intracellular domain of CD56 regulates actin and filopodia homeostasis. (A) WT or CD56-KO NK92 cells were incubated on anti-CD18/-NKp30 then fixed and immunostained for actin (phalloidin) and imaged by three-dimensional-SIM. Scale bar 5 μm. Representative of 43 cells (WT) and 44 cells (CD56-KO) from three technical replicates. (B) Three-dimensional reconstruction and XZ view of cells imaged as in (A). Inset highlights depths of actin accumulation. (C) Flow cytometry of cell surface CD56 expression. Representative of three technical replicates. (D) Western blot of CD56/NCAM with actin as a loading control. Representative of three technical replicates. (E) WT or CD56-KO NK92 or CD56-KO reconstituted with full-length or delta ICD CD56 were incubated on anti-CD18/-NKp30 then fixed, immunostained for actin (phalloidin) and imaged by SIM. Scale bar 5 μm. (F) Foci size and filopodia length were quantified for cell lines shown in (E). Each datapoint represents a foci or filopodia measurement. Foci $n = 183$ (WT), 225 (FL), 229 (KO), 215 (delta ICD); filopodia $n = 192$ (WT), 221 (full-length, FL), 204 (KO), 206 (delta intracellular domain, delta ICD) from 43 cells (WT) and 44 cells (CD56-KO) from three technical replicates. Large symbols indicate the mean from individual experiments coded by color, bars indicate median values of all points. ****$p < 0.0001$, ordinary one-way ANOVA with multiple comparisons.

DISCUSSION

Previous studies of the role of CD56/NCAM in human NK cell function indicated a role for CD56/NCAM in cell migration on stromal cells. Specifically, CD56/NCAM was found localized to the cell uropod of primary NK cells migrating or arrested on stroma (Mace et al., 2016). Deletion of CD56/NCAM in the NK92 cell line also impaired cell migration on stroma, suggesting that CD56/NCAM mediates NK-stromal cell interactions to promote motility of NK cells. Our current study advances previous studies of the role of CD56 in NK cell migration by demonstrating that CD56-deficient cells have impaired cell migration on the integrin ligand ICAM-1, and that loss of CD56/NCAM leads to impaired sustained cell polarity and increased detection of activated LFA-1 at the plane of activation on functionalized glass. This phenotype is accompanied by a striking actin cytoskeleton profile including enlarged actin foci and elongated filopodia present following ICAM-1 ligation by LFA-1 or integrin activation by antibody cross-linking. CD56/NCAM-deficient NK92 cells migrating on ICAM-1 had intact actin flow speed and amount of immobile actin but actin remodeling was not maintained with persistent directionality, resulting in multidirectional, short lived lamellipodia. As we do not predict that CD56/NCAM is binding directly to ICAM-1, this phenotype following CD56 deletion suggests that CD56/NCAM instead modulates actin responses by interacting with integrins or other receptors that modulate actin.

While we have previously shown that adhesion to target cells is unaffected in CD56-KO NK92 cells (Gunesch et al., 2020), directionality of actin flow in CD56-KO cells was highly irregular while flow speed was the same, indicating the significant role of actin dynamics in impaired cell migration in the absence of CD56. Further, establishment of cell polarity as indicated by ERM phosphorylation and capping was also largely intact, suggesting that the root cause of impairment in forward cell migration may be further downstream. Interestingly, the actin phenotype that we observed, namely large foci in CD56-deficient cells, was also present in cells which had undergone symmetrical spreading, indicating that integrin turnover is occurring in the absence of forward cell movement.

While phosphorylation of Pyk2 is globally decreased in CD56-KO NK cells (Gunesch et al., 2020), we now demonstrate that this global decrease in Pyk2 phosphorylation is associated with increased segregation of Pyk2 phospho-Y402 in enlarged actin complexes found in CD56/NCAM-KO cells. We further demonstrate that, as in T-cells (Cheung and Ostergaard, 2016), Pyk2 phospho-Y881 in migrating human NK cells preferentially localizes to the cell uropod, where it is more diffusely distributed in CD56-KO than WT cells. The mechanism by which NCAM regulates the interplay between integrin, actin, and cell migration is still unclear. The phenotype that we observe, namely of multiple leading edges formed as cells try to migrate but are unable to detach their uropod, is highly reminiscent of T-cells treated with Pyk2 inhibitor or dominant negative C-terminal FAT domain of Pyk2 (Cheung and Ostergaard, 2016). Together with previous reports showing Pyk2 phosphorylation in response to CD56 cross-linking in human NK cells (Picard et al., 2022), this data supports a role for CD56/NCAM in mediating signaling through Pyk2, including uropod detachment. Pyk2$^{-/-}$ macrophages have impaired chemokine-induced migration that includes impaired trailing edge detachment, further implicating Pyk2 function in cell detachment during migration and generating a cell phenotype resembling that seen in CD56-deficient NK cells (Okigaki et al., 2003). In neurons, CD56/NCAM binds directly to the Src family kinase member Fyn through the NCAM-140 intracellular domain and mediates FAK signaling in lipid rafts (Beggs et al., 1997; Niethammer et al., 2002). Here we show that the intracellular

domain of CD56/NCAM is required for its function, suggesting that steric hindrance by polysialated CD56/NCAM on the cell surface is not primarily the mechanism by which CD56/NCAM regulates integrin function. CD56/NCAM may act similarly in lymphocytes to regulate interactions between Fyn, Pyk2, and integrins which are required for actin homeostasis.

While actin flow speed in CD56-KO NK92 cells is minimally affected, CD56-KO NK92 cells form multipolar phenotypes in response to integrin ligation and demonstrate impaired uropod retraction and forward movement. This phenotype suggests that the actin phenotype that we observe, namely enlarged actin clusters and long filopodia, results from reduced Pyk2 phosphorylation and Pyk2 mislocalization. Actin regulation requires the intracellular domain of CD56/NCAM, suggesting that it is not simply steric modulation via polysialated CD56/NCAM. However, whether CD56/NCAM can play a similar role in the arrangement of other cell surface receptors remains to be seen and may be related to previously reported defects in cytotoxic function and cytokine secretion by CD56-deficient human NK cells. Recent studies of CD44 have identified its role in modulating the macrophage glycocalyx by acting as a picket protein (Freeman et al., 2018), and it is conceivable that CD56/NCAM could serve a similar function. Similar studies have identified integrins as subject to glycocalyx regulation (Paszek et al., 2014), however single molecule studies of CD56/NCAM, Pyk2 and integrins are required to fully elucidate the relationship between them.

The function of CD56/NCAM has been difficult to fully elucidate, likely in part because it is not acting in conventional receptor-ligand interactions. Regulation of integrin detachment enables cell migration on two-dimensional surfaces, and impaired integrin inactivation or integrin endocytosis following ligand binding prevents cell migration (Fabbri et al., 1999; Tohyama et al., 2003; Rantala et al., 2011). While our studies were primarily performed on ICAM-1 coated surfaces, there is no indication that CD56/NCAM is directly binding to ICAM-1, as large actin foci and elongated filopodia were also present in response to anti-CD18 cross-linking. The use of isolated ligands in the current study also avoids the potential binding of CD56/NCAM to other NCAM molecules present on stromal cells previously used to measure NK cell migration (Mace et al., 2016), convincingly ruling out NCAM-NCAM interactions as the mediators of CD56-dependent cell migration on stromal cells. While not previously shown in NK cells, cell adhesion molecules can mediate integrin detachment and turnover. L1CAM, which is structurally similar to NCAM, promotes endocytosis of integrin β1 to enable forward cell migration (Panicker et al., 2006). Whether CD56/NCAM promotes appropriate initial integrin binding and receptor engagement or functions solely in detachment via deactivation or endocytosis, remains to be seen. Interestingly, in our previous studies of the role of CD56/NCAM in NK cell immunological synapse formation and function, we noted increased frequency of NK-target cell conjugates in the absence of CD56 function (Gunesch et al., 2020). While not explicitly confirmed, the data from our current study suggests that impaired deadhesion or LFA-1 turnover may underlie the increased adhesion of NK cells to targets.

Many interesting questions remain about the biological function of CD56/NCAM, including the way in which human NK cell subsets with different densities of CD56/NCAM undergo cell migration and the single-molecule dynamics of CD56 during migration. In addition to differences in CD56 density, human NK cell subsets have extensive differences in actin and integrin machinery (Hegewisch-Solloa et al., 2021). While acute loss of CD56/NCAM in NK cell lines with high CD56 expression, such as NK92 cells, leads to impaired cell migration, closer study of its role in other NK cell subsets will be
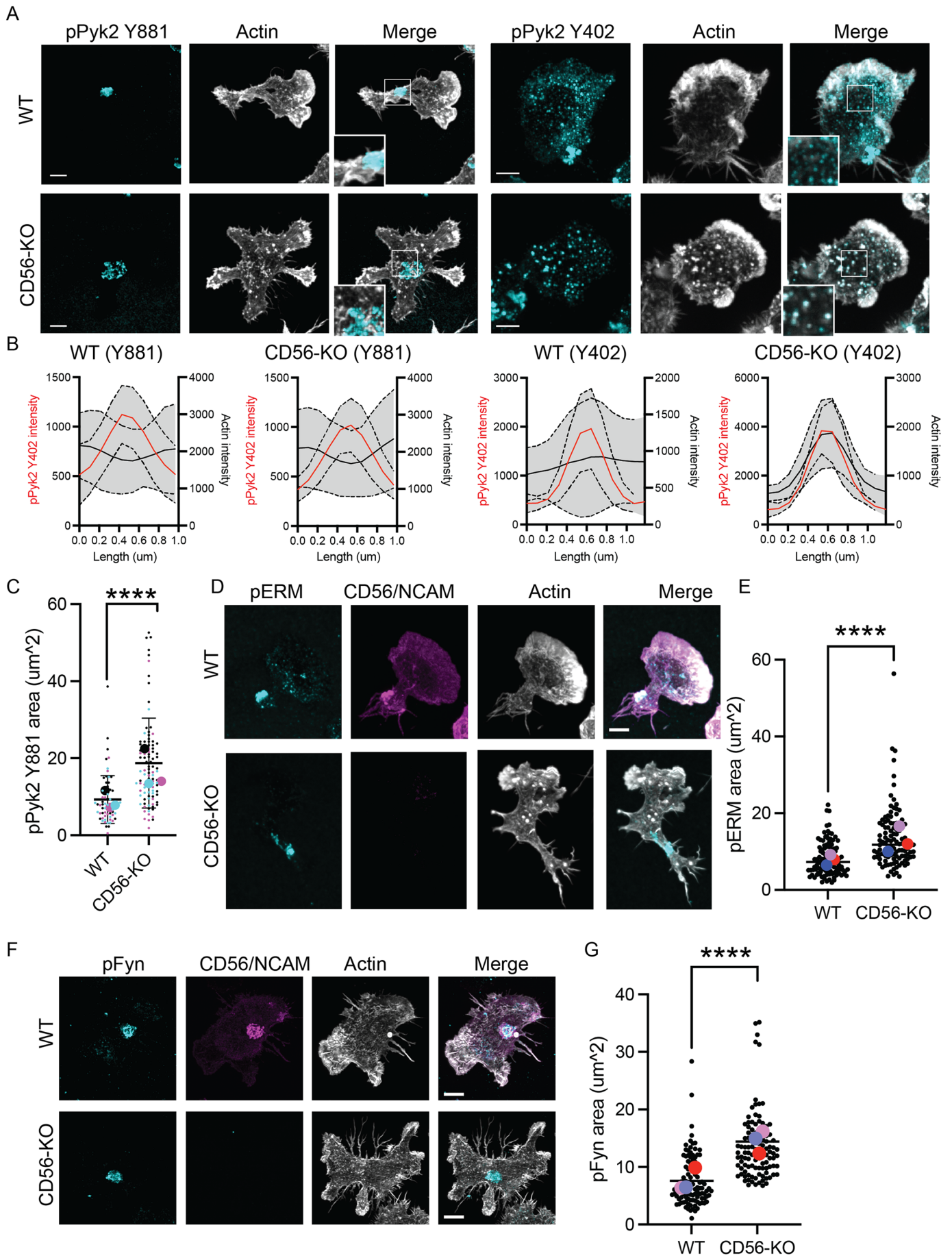
necessary to fully understand how it interacts with other signaling pathways that regulate cell migration. Similarly, the study of other immune cells that express CD56/NCAM, including NKT cells, myeloid precursors in mice, and transformed cells such as myeloma, remains an interesting area of further study. Conversely, a deeper understanding of the function of CD56/NCAM will shed light on the significance of its relative expression levels given the high density on CD56^{bright} NK cells, low density on CD56^{dim} NK cells, and absence on murine NK cells and other human lymphocyte subsets. The identity of other molecules that may play a similar role on cells that do not normally express CD56/NCAM, including T-cells and murine NK cells, is not known. In addition to CD56/NCAM, other Ig superfamily adhesion receptors that may regulate adhesion and actin remodeling on immune cells include CD2 (Binder *et al.*, 2020), CD58 (Binder *et al.*, 2020), and nectins (Samanta and Almo, 2015). The mechanism by which functional redundancy between these molecules could occur, including the consequence of CD56/NCAM downregulation in NK cell maturation or in response to chronic viral infection (Mavilio *et al.*, 2005), is an interesting area for further investigation. Finally, it must be noted that the current studies were performed on two-dimensional surfaces in the absence of shear flow, and it will be of interest to further understand how CD56/NCAM-deficient cells interact with three-dimensional and complex microenvironments. Nevertheless, our current study sheds light on the cell biological function of a ubiquitously expressed but poorly understood receptor on human immune cells and its function in cell migration.

MATERIALS AND METHODS
Request a protocol through *Bio-protocol.*

Cell lines and cell culture
NK92 cells were purchased from ATCC (CRL-2407) and monitored monthly by flow cytometry for CD56 expression and other markers of NK cell identity. CD56-KO cells were generated and validated as described previously (Mace *et al.*, 2016). WT, CD56-KO, and LifeAct-mScarlet NK92 cells were maintained in culture in MEM alpha medium without ribonucleosides and deoxyribonucleosides but with 2 mM L-glutamine and 1.5 g/L sodium bicarbonate (Life Technologies; 12-561-056), supplemented with 12.5% fetal bovine serum (FBS), 12.5% horse serum, 100 U/ml IL-2 (ProLeukin; 65483-116-07), 200 µM myoinositol (Thermo J62886.22), 20 µM folic acid

(Sigma F8758-25G), 100 µM 2-mercaptoethanol (Life Technologies; 21985-023) and 1% Pen-Strep antibiotics. pLifeAct_mScarlet_N1 was a gift from Dorus Gadella (Addgene plasmid # 85054; RRID:Addgene_85054). WT and CD56-KO NK92 cells were nucleofected with pLifeAct mScarlet using an Amaxa nucleofector (Kit R) and cells were selected with G418 before validating expression by microscopy and flow cytometry. Cells were monitored for mycoplasma contamination by monthly testing.

Flow cytometry
Flow cytometry was performed on cell lines as independent technical replicates with different passages of cells on different days. NK92 cells were harvested, washed once with complete media and resuspended in PBS for immunostaining. Cells were incubated with FITC anti-CD18 (clone 6.7, BD Biosciences, 1:100) for 30 min at 4C in the dark then washed once with PBS. Fluorescence minus one controls were prepared for CD18 conditions. Data were acquired on a BD Fortessa cytometer and exported to FlowJo (BD Biosciences) for analysis and graphed with Prism 8.0 (GraphPad).

Lysate preparation and Western blots
Cell lysates from 3×10^6 cells were generated using RIPA Lysis and Extraction Buffer (Thermo Fisher Scientific; 89901) supplemented with 1X Halt protease inhibitor cocktail (Thermo Fisher Scientific; 78443). Samples were incubated at 95°C with NuPAGE sample reducing agent (Thermo Fisher Scientific; NP0004) andNuPAGE LDS sample buffer (Thermo Fisher Scientific; NP0007) for 10 min. 5×10^5 cell equivalents per well were loaded into a NuPAGE 4–12% Bis-Tris density gradient gel (Thermo Fisher Scientific; NP0432) and ran at a constant 150V for 80 min. Separated proteins were transferred onto nitrocellulose membranes at a constant 0.2A for 90 min. The nitrocellulose membranes were then blocked with 5% nonfat milk in PBS 0.05% Tween-20 for 60 min at 4°C. Nitrocellulose membranes were incubated overnight at 4°C with primary antibodies in 5% (wt/vol) BSA in PBS 0.05% Tween 20 at the following dilutions: 1:1000 anti-CD56 (clone 123C3; Cell Signaling Technology; 3576) and 1:4000 anti-actin (polyclonal; Sigma-Aldrich; A2066) as a loading control. Membranes were washed with 0.5 M NaCl in PBS 0.05% Tween 20. Primary antibodies were probed with IRDye 680RD Goat antimouse IgG (Licor Biosciences; 926-68070) or IRDye 800CW goat antirabbit IgG (Li-COR Biosciences; 926-32211) secondary antibodies 1:10,000 for 1 h at

---

FIGURE 5: pPyk2 localization is dysregulated in CD56-KO NK92 cells. (A) WT and CD56-KO NK92 cells were incubated on ICAM-1 coated surfaces for 45 min then fixed and immunostained for actin (phalloidin) and Pyk2 phospho-Y881 or phospho-Y402 as indicated. Maximum projection images are shown. 2X magnification shown in inset. Representative images from 30 (WT) and 29 (CD56-KO) phospho-Y402 fields of view from three technical replicates; Pyk2 phospho-Y881 representative images from 45 WT or CD56-KO cells from four technical replicates. (B) Line profiles drawn across actin foci in WT or CD56-KO NK92 cells were used to generate actin intensity (black line) are shown with corresponding Pyk2 phospho-Y402 or Pyk2 phospho-Y881 intensity (red line). $n = 10$ foci per condition from one representative experiment from four technical replicates. Solid line, mean; dashed line, SD. (C) Quantification of area of pPyk2 Y881 immunofluorescence quantified from maximum projection images. Each datapoint is a cell. $n = 67$ (WT), 103 (CD56-KO) from three independent experiments coded by color, large symbols indicate the mean from individual experiments, bars and error bars are mean $\pm$ SD of all points. (D) Cells were treated as in (A) and immunostained for phospho-ERM. Representative maximum projections are shown. Scale bar 5 µm. (E) Quantification of area of pERM immunofluorescence quantified from maximum projection images. Each datapoint is a single cell. $n = 107$ (WT), 108 (CD56-KO) from three independent experiments coded by color, large symbols indicate the mean from individual experiments, bars indicate median values of all points. ****$p < 0.0001$ by Mann-Whitney test. (F) Cells were treated as in (A) and immunostained for phospho-Fyn. Representative maximum projections are shown. Scale bar 5 µm. (G) Quantification of area of phospho-Fyn immunofluorescence quantified from maximum projection images. Each datapoint is a single cell. $N = 104$ (WT), 108 (CD56-KO) from three independent experiments coded by color, large symbols indicate the mean from individual experiments, bars indicate median values of all points. ****$p < 0.0001$ by Mann-Whitney test.
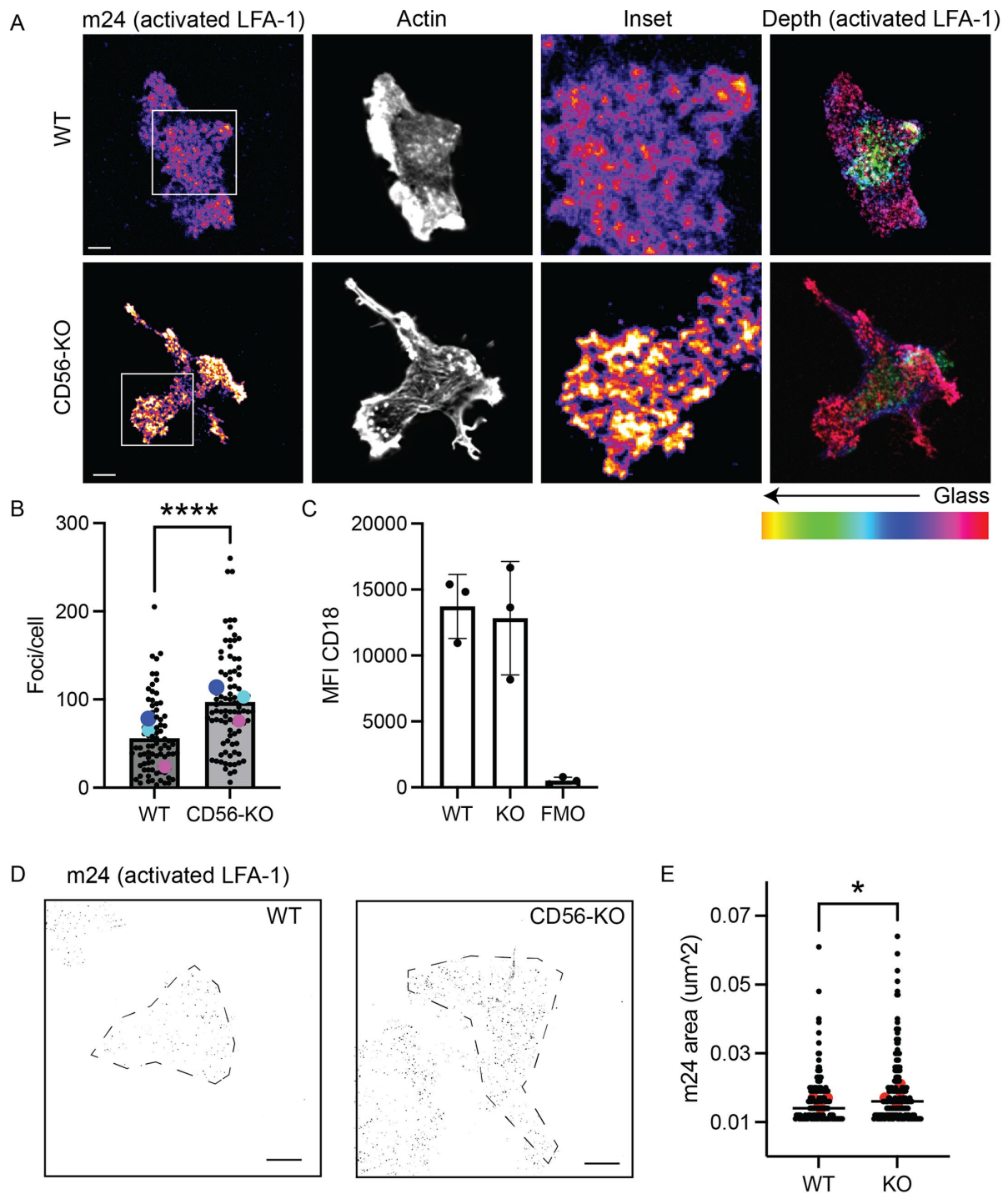
FIGURE 6: Increased LFA-1 activation in CD56-KO NK92 cells on ICAM-1. (A) WT and CD56-KO NK92 cells were incubated on ICAM-1 coated surfaces for 45 min then fixed and immunostained for actin (phalloidin) and open conformation LFA-1 (clone m24) as indicated and imaged by confocal microscopy. Depth color shading of Z stacks taken throughout the image is shown to the right, all other images are a single plane of the cell proximal to the glass. Representative images from 41 fields of view (WT or CD56-KO) from three technical replicates. Scale bar 5 µm. (B) Quantification of the frequency of m24 foci/ per cell shown with the average from each experiment coded by color. $n = 83$ (WT), 90 (CD56-KO) from three technical replicates, bars show mean values of all points. ****$p < 0.0001$ by Mann-Whitney test. C) MFI of surface expression of integrin β2 (CD18) on WT and CD56-KO NK92 cells measured by flow cytometry; FMO, fluorescence minus one control. $n = 3$ independent technical replicates, mean ± SD. (D) Visualization of m24 prepared as in (A) and imaged by three-dimensional-SIM. Images shown are maximum project of three slices at the plane of the glass. Scale bar 5 µm; cell footprint outlined by dashed line. (E) Quantification of the area of m24 immunofluorescence of individual foci from SIM microscopy data. Representative data from three independent experiments, $n = 4$ (WT), 5 (KO) cells. Each black symbol is a single foci, each red symbol is the mean of a single cell, bars indicate median. *$p < 0.05$ by Mann-Whitney test.

room temperature. Nitrocellulose membranes were imaged using the Odyssey CLx imaging system (Li-COR Biosciences).

Sample preparation for live cell imaging

Glass chamber slides were coated with 0.001% Poly L-Lysine (PLL; Sigma P4707) for 1 h at room temperature, washed five times with PBS, and then coated with a solution of PBS containing 5 µg/ml fc-ICAM-1 (R&D; 720-IC-200), anti-CD18 (purified from hybridoma; clone TS1/18), or 5 µg/ml Control:Fc (Enzo Life Science; ALX-203-004-C050) overnight at 4°C. Each well was then washed three times with cell culture media. WT or CD56-KO NK92 cells were counted, centrifuged at 300 g for 3 min, washed with media, and centrifuged for a further 3 min at 300 g before being resuspended in media. 5×10^4 cells were added to each well and cells were incubated at 37°C in the presence of 5% CO_2 on the microscope for 1 h to adhere cells to the surface before imaging.

Confocal microscopy

WT and CD56-KO NK92 cells were incubated for 30 min (antibody coating) or 45 min (Fc-ICAM coating) at 37°C and 5% CO_2 on #1.5 glass coverslips that had been precoated with 10 µg/ml anti-CD18 (clone IB4) and anti-NKp30 (clone P30-15, Biolegend; 325202) or 5 µg/ml Fc-ICAM-1 (Enzo Life Science; ALX-203-004-C050). NK cells were fixed and permeabilized with CytoFix/CytoPerm (BD Biosciences; 554714) at room temperature for 20 min. Fixative was removed and coverslips were rinsed three times with 150 µl PBS 1% BSA 0.1% saponin. The following antibodies and reagents were used for fixed cell staining at 1:100 dilutions: phalloidin Alexa Fluor 568 (Thermo Fisher Scientific; A12380), CD56 Alexa Fluor 647 (clone HCD56; Biolegend; 318314), CD44 Alexa Fluor 488 (clone C44Mab-5; Biolegend; 397508), open conformation LFA-1 Alexa Fluor 488 (clone m24; Biolegend; 363404), phospho-Pyk2 (Tyr402; polyclonal; Abcam; ab4800), phospho-Pyk2 (Tyr881; polyclonal; Abcam; ab4801), phospho-ezrin/radixin/moesin (Thr558; polyclonal; Thermo Fisher Scientific; PA5-38679), phospho-Fyn (Tyr530; polyclonal; Thermo Fisher Scientific; PA5-104756), goat antimouse IgG (H+L) cross-adsorbed secondary antibody Alexa Fluor 488 (polyclonal; Thermo Fisher Scientific; A-11001), goat antirabbit IgG (H+L) cross-adsorbed secondary antibody Alexa Fluor 488 (polyclonal; Thermo Fisher Scientific; A-11008). Coverslips were mounted on slides with ProLong Glass antifade reagent (Thermo Fisher Scientific; P36934). Images were acquired with a 100 × 1.46 NA objective on a Zeiss AxioObserver Z1 microscope stand equipped with a Yokogawa W1 spinning disk. Illumination was by solid state laser and detection by Prime 95B sCMOS camera. Data were acquired in SlideBook software (Version 6, Intelligent Imaging Innovations) and exported as TIFF files for further analysis. Live actin imaging was performed using confocal imaging on the same system. Timelapse images of a single axial plane close to the coverslip were acquired every 1 s for 120 s per cell. Laser power was set at 20% with integration time of 50 ms using a 561-nm laser and associated filters. Low resolution phase contrast imaging was performed using the same microscope with a 20 × 0.5 NA magnification lens. Images were captured every 10 s for 30 min. For cytochalasin D treatment, cells were incubated on functionalized surfaces for 20 min before addition of cytochalasin D (Abcam; ab143484) to a final concentration of 2 µM then incubated for 10 min before imaging. An environmental chamber maintained consistent 5% CO_2 and 37°C (OKOlab).

Structured illumination microscopy (SIM)

WT and CD56-KO NK92 cells were prepared as described for confocal microscopy. Images were acquired on a GE Deltavision OMX SR equipped with a 60 × 1.42 NA APO objective and three PCO Chip sCMOS cameras. Three-dimensional images were captured with 0.125 µm steps with a pixel size of 0.079 µm. SIM images were reconstructed with GE SoftWoRX software using three orientations and five phase shifts with a Wiener filter constant of 0.005 and negative values not discarded.

Lattice lightsheet microscopy

WT and CD56-KO LifeAct mScarlet NK92 cells were resuspended in low serum NK92 media and then mixed with collagen that had been neutralized with sodium bicarbonate buffer for a final collagen concentration of 1.6 mg/ml. Cells and collagen were incubated for 90 min in an Ibidi microchannel slide with #1.5 glass bottom. Cells were imaged on a Zeiss Lattice Lightsheet microscope with environmental control maintaining 37°C and 5% CO_2. Cells were imaged at 20-s intervals for 20–30 min. Deconvolution by constrained iterative algorithm and deskewing was performed using Zen (Zeiss Microsystems).

Cell tracking analysis

Custom Fiji macros were used to organize TIFF stacks exported from SlideBook software into time-discriminated TIFF image sequences in replicate and condition folder hierarchy (Shannon *et al.*, 2023). Images were segmented using the Cyto2 trained network provided by Cellpose (Stringer *et al.*, 2021) using a classification object diameter of 30 pixels for data acquired at 20X magnification and 150 pixels for data acquired at 100X magnification and was run from the Anaconda command line. Bayesian Tracker (Ulicna *et al.*, 2021) was used to track segmented cells between frames and was run through a custom, generalizable Jupyter Notebook script (Shannon *et al.*, 2023). A HDF5 file containing segmented masks and tracks for each cell was output for each TIFF stack replicate and saved in the folder hierarchy. Custom Python functions were used to make 30 separate shape, migration, and clustering measurements per timepoint per cell and save these in a large Pandas dataframe containing all conditions and all replicates for each experiment (Shannon *et al.*, 2023). Migration measurements were mostly made between adjacent frames, but some measurements were normalized over 60-s time windows to compare tracks of different lengths; namely Euclidean distance, cumulative distance, and arrest coefficient. The radius r used for Ripley's L(r) was 13.5 µm, 1.5X the average diameter of a single cell. Data was filtered to exclude objects smaller than 10 µm^2 and cells tracked for fewer than 12 frames (120 s) for 20X data and 120 frames (120 s) for 100X data as they were assumed to be floating debris.

Confocal microscopy data processing and analysis

Line profiles were generated on single cells that had polarized in response to incubation on ICAM-1. Polarized cells were identified by the accumulation of CD44, and line profiles were generated while blinded to CD56 distribution to avoid selection bias of cells for analysis. For quantitative analysis of CD56 and CD44 polarization, equal-sized regions of interest were measured at the leading edge or uropod of primary NK cells polarized on ICAM-1. For line profiles of pPyk2 staining, 1-µm line profiles were centered on pPyk2 foci and MFI was measured along the line. Actin MFI was measured along the same line and MFI was plotted for each channel for 10 line profiles.

Foci analysis of m24, pERM, and pFyn was performed in Fiji (Schindelin *et al.*, 2012). Single slices at the plane of the glass (SIM data) or maximum projection (confocal data) were selected using the actin (phalloidin) channel to delineate the plane of contact with glass and the boundaries of individual cells. Thresholding was performed

based on a value that excluded background from outside the cell and the threshold value was consistent between cells in all conditions from a given experiment. For foci, Measure Particles was used with a size exclusion lower limit of 0.01 μm^2 and no upper limit or circularity restriction. For area of immunofluorescence, the Measure tool was used with "Limit to threshold" selected. Area of individual foci and frequencies (numbers of foci per cell) were plotted in Prism (GraphPad Software) using SuperPlots (Lord *et al.*, 2020; Goedhart, 2021), where the mean from each individual technical replicate is shown as a large symbol and individual datapoints are shown as small datapoints with individual technical replicates coded by color. Counting of lamellipodia (Figure 3H) was performed by manual counting of fixed cell confocal microscopy images by an observer blinded to experimental conditions. Lamellipodia were scored by the presence of a clear leading edge. Cells were scored as zero when no clear leading edges were observed. The number of cells with 0, 1, or >1 leading edges were counted and expressed as a fraction of the number of cells from the experiment being quantified. These fractions were graphed from three independent technical replicates.

Plotting and statistical analysis

Due to a high volume of data, *p* values from automated live cell tracking were in some cases very small. We sought to display the effect size to better understand comparisons between conditions. Plots of Difference (Goedhart, 2019) were adapted for Python and Matlab (from R) and used to calculate the effect size distribution. Briefly, data were bootstrapped by repeatedly sampling (1000 times with replacement) to generate many new samples of the same size and a distribution of medians for each sample. Effect size distribution was calculated by subtracting each control condition bootstrapped median from the bootstrapped median of each respective condition. This distribution was then used to estimate the variability of the median, allowing us to assess the statistical significance of differences between conditions in the dataset. This approach quantifies how much the median of a given factor (like a measurement or outcome) differs between each condition and the control, accounting for variability in those estimates through the bootstrapping process. Visually, the median effect size and confidence intervals and their distance from the control condition indicate the biological and statistical significance of the change respectively and a tight distribution far away from the control line indicates significance. *P* values were calculated using the randomization method, making no assumption about the underlying data distribution (Nuzzo, 2017). Superplots of Data (Goedhart, 2021) were also adapted for Python and Matlab (from R) and used to transparently display data from individual replicates and individual conditions.

Statistical comparisons were performed in Prism (Graphpad Software). Datasets were tested for normal distribution. If normal distribution was not detected, unpaired datasets were compared by Mann-Whitney test. Paired data with nonnormal distribution were compared with Wilcoxan matched-pairs signed rank test. For multiple comparisons, data were compared by one-way ANOVA with multiple comparisons; stacked bar plots were compared with Sidak's multiple comparisons test. No data were excluded from analysis.

Optical flow analysis

Images were exported from Slidebook software as TIFF stacks. FIJI was used to preselect cells with average intensity >300, indicating the presence of enough tagged actin on which to perform optical flow analysis. FIJI was also used to order the files into folders for batch analysis. To measure the magnitude and directionality of actin flow, we adapted an algorithm based on the Lucas-Kanade method (Oveisi *et al.*, 2018), which calculates vectors for flows of "like" pixel intensities detected between subsequent frames. The x/y vector components are used to generate vector maps encoding the magnitude and directionality of flow. Masks based on the cell contour and a reliability matrix for each vector based on properties of the underlying image was used to remove noise. A lower reliability threshold of 0.01 times the maximum reliability value for each individual cell was used to select reliable vectors. The number of pixels with no reliable vectors or vectors below a lower magnitude threshold of 0.5 μm/min were classed as immobile and were divided by the total number of pixels within the cell to give the immobile fraction per time point. The distribution of flow vectors for overlapping time windows of 10 frames (10 s) were fit to a von Mises distribution, and the kappa parameter was used to indicate the persistence of motion of flow in a single direction (Lee *et al.*, 2020b). Higher kappa values indicated more persistently directional flow. Batch analysis of cells in folders and output of all plots is possible by changing a single directory line, pixel size, and time between frames in the code provided by Dr. Arpita Upadhyaya that is available at https://zenodo.org/record/8221517.

Code availability

Optical flow analysis software was kindly provided by Dr. Ivan Rey-Suarez (Upadhyaya Lab) and was adapted here for batch analysis and plotting of actin flow speed, Von Mises persistence of motion, and calculation of the immobile fraction. This version of the software is available at https://zenodo.org/record/8221517. Calculations of migration characteristics, cell clustering and morphology per cell per time point, including Plots of Difference (Goedhart, 2019), Time-Plots of Difference, and SuperPlots (Lord *et al.*, 2020; Goedhart, 2021) were created using cellPLATO (Shannon *et al.*, 2023) with code available at https://zenodo.org/records/8096717.

REFERENCES

Beggs HE, Baragona SC, Hemperly JJ, Maness PF (1997). NCAM140 interacts with the focal adhesion kinase p125(fak) and the SRC-related tyrosine kinase p59(fyn). J Biol Chem 272, 8310–8319.

Bindels DS, Haarbosch L, van Weeren L, Postma M, Wiese KE, Mastop M, Aumonier S, Gotthard G, Royant A, Hink MA, Gadella TW, Jr. (2017). mScarlet: a bright monomeric red fluorescent protein for cellular imaging. Nat Methods 14, 53–56.

Binder C, Cvetkovski F, Sellberg F, Berg S, Paternina Visbal H, Sachs DH, Berglund E, Berglund D (2020). CD2 Immunobiology. Front Immunol 11, 1090.

Charbord P, Oostendorp R, Pang W, Herault O, Noel F, Tsuji T, Dzierzak E, Peault B (2002). Comparative study of stromal cell lines derived from embryonic, fetal, and postnatal mouse blood-forming tissues. Exp Hematol 30, 1202–1210.

Cheung SM, Ostergaard HL (2016). Pyk2 controls integrin-dependent ctl migration through regulation of de-adhesion. J Immunol 197, 1945–1956.

Culley FJ, Johnson M, Evans JH, Kumar S, Crilly R, Casasbuenas J, Schnyder T, Mehrabi M, Deonarain MP, Ushakov DS, *et al.* (2009). Natural killer cell signal integration balances synapse symmetry and migration. PLoS Biol 7, e1000159.

Dupre L, Houmadi R, Tang C, Rey-Barroso J (2015). T Lymphocyte migration: An action movie starring the actin and associated actors. Front Immunol 6, 586.

Fabbri M, Fumagalli L, Bossi G, Bianchi E, Bender JR, Pardi R (1999). A tyrosine-based sorting signal in the beta2 integrin cytoplasmic domain mediates its recycling to the plasma membrane and is required for ligand-supported migration. EMBO J 18, 4915–4925.

Freeman SA, Vega A, Riedl M, Collins RF, Ostrowski PP, Woods EC, Bertozzi CR, Tammi MI, Lidke DS, Johnson P, *et al.* (2018). Transmembrane pickets connect cyto- and pericellular skeletons forming barriers to receptor engagement. Cell 172, 305–317 e310.

Goedhart J (2019). PlotsOfDifferences – A web app for the quantitative comparison of unpaired data. bioRxiv, https://doi.org/10.1101/578575.

Goedhart J (2021). SuperPlotsOfData-a web app for the transparent display and quantitative comparison of continuous data from different conditions. Mol Biol Cell 32, 470–474.

Gunesch JT, Dixon AL, Ebrahim TA, Berrien-Elliott MM, Tatineni S, Kumar T, Hegewisch-Solloa E, Fehniger TA, Mace EM (2020). CD56 regulates human NK cell cytotoxicity through Pyk2. eLife 9, e57346.

Hegewisch-Solloa E, Seo S, Mundy-Bosse BL, Mishra A, Waldman EH, Maurrasse S, Grunstein E, Connors TJ, Freud AG, Mace EM (2021). Differential integrin adhesome expression defines human NK cell residency and developmental stage. J Immunol 207, 950–965.

Kumari S, Mak M, Poh YC, Tohme M, Watson N, Melo M, Janssen E, Dustin M, Geha R, Irvine DJ (2020). Cytoskeletal tension actively sustains the migratory T-cell synaptic contact. EMBO J 39, e102783.

Lanier LL, Chang C, Azuma M, Ruitenberg JJ, Hemperly JJ, Phillips JH (1991). Molecular and functional analysis of human natural killer cell-associated neural cell adhesion molecule (N-CAM/CD56). J Immunol 146, 4421–4426.

Lanier LL, Testi R, Bindl J, Phillips JH (1989). Identity of Leu-19 (CD56) leukocyte differentiation antigen and neural cell adhesion molecule. J Exp Med 169, 2233–2238.

Lee BJ, Hegewisch Solloa E, Shannon MJ, Mace EM (2020a). Generation of cell-derived matrices that support human NK cell migration and differentiation. J Leukoc Biol 108, 1369–1378.

Lee BJ, Mace EM (2017). Acquisition of cell migration defines NK cell differentiation from hematopoietic stem cell precursors. Mol Biol Cell 28, 3573–3581.

Lee RM, Campanello L, Hourwitz MJ, Alvarez P, Omidvar A, Fourkas JT, Losert W (2020b). Quantifying topography-guided actin dynamics across scales using optical flow. Mol Biol Cell 31, 1753–1764.

Lord SJ, Velle KB, Mullins RD, Fritz-Laylin LK (2020). SuperPlots: Communicating reproducibility and variability in cell biology. J Cell Biol 219, e202001064.

Lowin-Kropf B, Kunz B, Schneider P, Held W (2002). A role for the src family kinase Fyn in NK cell activation and the formation of the repertoire of Ly49 receptors. Eur J Immunol 32, 773–782.

Mace EM, Gunesch JT, Dixon A, Orange JS (2016). Human NK cell development requires CD56-mediated motility and formation of the developmental synapse. Nat Commun 7, 12171.

Mavilio D, Lombardo G, Benjamin J, Kim D, Follman D, Marcenaro E, O'Shea MA, Kinter A, Kovacs C, Moretta A, Fauci AS (2005). Characterization of CD56-/CD16+ natural killer (NK) cells: A highly dysfunctional NK subset expanded in HIV-infected viremic individuals. Proc Natl Acad Sci USA 102, 2886–2891.

Moebius JM, Widera D, Schmitz J, Kaltschmidt C, Piechaczek C (2007). Impact of polysialylated CD56 on natural killer cell cytotoxicity. BMC Immunol 8, 13.

Mrass P, Kinjyo I, Ng LG, Reiner SL, Pure E, Weninger W (2008). CD44 mediates successful interstitial navigation by killer T cells and enables efficient antitumor immunity. Immunity 29, 971–985.

Niethammer P, Delling M, Sytnyk V, Dityatev A, Fukami K, Schachner M (2002). Cosignaling of NCAM via lipid rafts and the FGF receptor is required for neuritogenesis. J Cell Biol 157, 521–532.

Nuzzo RL (2017). Randomization Test: An alternative analysis for the difference of two means. PM R 9, 306–310.

Okigaki M, Davis C, Falasca M, Harroch S, Felsenfeld DP, Sheetz MP, Schlessinger J (2003). Pyk2 regulates multiple signaling events crucial for macrophage morphology and migration. Proc Natl Acad Sci USA 100, 10740–10745.

Oveisi E, Letouzey A, De Zanet S, Lucas G, Cantoni M, Fua P, Hebert C (2018). Stereo-vision three-dimensional reconstruction of curvilinear structures imaged with a TEM. Ultramicroscopy 184, 116–124.

Panicker AK, Buhusi M, Erickson A, Maness PF (2006). Endocytosis of beta1 integrins is an early event in migration promoted by the cell adhesion molecule L1. Exp Cell Res 312, 299–307.

Paszek MJ, DuFort CC, Rossier O, Bainer R, Mouw JK, Godula K, Hudak JE, Lakins JN, Wijekoon AC, Cassereau L, *et al.* (2014). The cancer glycocalyx mechanically primes integrin-mediated growth and survival. Nature 511, 319–325.

Picard LK, Claus M, Fasbender F, Watzl C (2022). Human NK cells responses are enhanced by CD56 engagement. Eur J Immunol 52, 1441–1451.

Rak GD, Mace EM, Banerjee PP, Svitkina T, Orange JS (2011). Natural killer cell lytic granule secretion occurs through a pervasive actin network at the immune synapse. PLoS Biol 9, e1001151.

Rantala JK, Pouwels J, Pellinen T, Veltel S, Laasola P, Mattila E, Potter CS, Duffy T, Sundberg JP, Kallioniemi O, *et al.* (2011). SHARPIN is an endogenous inhibitor of beta1-integrin activation. Nat Cell Biol 13, 1315–1324.

Samanta D, Almo SC (2015). Nectin family of cell-adhesion molecules: structural and molecular aspects of function and specificity. Cell Mol Life Sci 72, 645–658.

Sancho D, Nieto M, Llano M, Rodriguez-Fernandez JL, Tejedor R, Avraham S, Cabanas C, Lopez-Botet M, Sanchez-Madrid F (2000). The tyrosine kinase PYK-2/RAFTK regulates natural killer (NK) cell cytotoxic response, and is translocated and activated upon specific target cell recognition and killing. J Cell Biol 149, 1249–1262.

Sandig M, Rao Y, Siu CH (1994). The homophilic binding site of the neural cell adhesion molecule NCAM is directly involved in promoting neurite outgrowth from cultured neural retinal cells. J Biol Chem 269, 14841–14848.

Schaeuble K, Hauser MA, Singer E, Groettrup M, Legler DF (2011). Cross-talk between TCR and CCR7 signaling sets a temporal threshold for enhanced T lymphocyte migration. J Immunol 187, 5645–5652.

Schindelin J, Arganda-Carreras I, Frise E, Kaynig V, Longair M, Pietzsch T, Preibisch S, Rueden C, Saalfeld S, Schmid B, *et al.* (2012). Fiji: An open-source platform for biological-image analysis. Nat Methods 9, 676–682.

Shannon MJ, Eisman SE, Lowe AR, Sloan T, Mace EM (2023). cellPLATO: An unsupervised method for identifying cell behaviour in heterogeneous cell trajectory data. bioRxiv, https://doi.org/10.1101/2023.10.28.564355.

Sims TN, Soos TJ, Xenias HS, Dubin-Thaler B, Hofman JM, Waite JC, Cameron TO, Thomas VK, Varma R, Wiggins CH, *et al.* (2007). Opposing effects of PKCtheta and WASp on symmetry breaking and relocation of the immunological synapse. Cell 129, 773–785.

Stringer C, Wang T, Michaelos M, Pachitariu M (2021). Cellpose: A generalist algorithm for cellular segmentation. Nat Methods 18, 100–106.

Sytnyk V, Leshchyns'ka I, Schachner M (2017). Neural cell adhesion molecules of the immunoglobulin superfamily regulate synapse formation, maintenance, and function. Trends Neurosci 40, 295–308.

Tohyama Y, Katagiri K, Pardi R, Lu C, Springer TA, Kinashi T (2003). The critical cytoplasmic regions of the alphaL/beta2 integrin in Rap1-induced adhesion and migration. Mol Biol Cell 14, 2570–2582.

Ulicna K, Vallardi G, Charras G, Lowe AR (2021). Automated deep lineage tree analysis using a bayesian single cell tracking approach. Front Comput Sci 3 e734559.

Wheatley BA, Rey-Suarez I, Hourwitz MJ, Kerr S, Shroff H, Fourkas JT, Upadhyaya A (2022). Nanotopography modulates cytoskeletal organization and dynamics during T cell activation. Mol Biol Cell 33, ar88.